
Solving Inverse Problems in Protein Space Using Diffusion-Based Priors

Axel Levy¹*
Stanford University

Eric R. Chan²
Stanford University

Sara Fridovich-Keil¹
Stanford University

Frédéric Poitevin³
SLAC National Accelerator Laboratory

Ellen D. Zhong⁴
Princeton University

Gordon Wetzstein¹*
Stanford University

axel-levy.github.io/adp-3d

Abstract

The interaction of a protein with its environment can be understood and controlled via its 3D structure. Experimental methods for protein structure determination, such as X-ray crystallography or cryogenic electron microscopy, shed light on biological processes but introduce challenging inverse problems. Learning-based approaches have emerged as accurate and efficient methods to solve these inverse problems for 3D structure determination, but are specialized for a predefined type of measurement. Here, we introduce a versatile framework to turn biophysical measurements, such as cryo-EM density maps, into 3D atomic models. Our method combines a physics-based forward model of the measurement process with a pretrained generative model providing a task-agnostic, data-driven prior. Our method outperforms posterior sampling baselines on linear and non-linear inverse problems. In particular, it is the first diffusion-based method for refining atomic models from cryo-EM maps and building atomic models from sparse distance matrices.

1 Introduction

Experimental methods in structural biology such as X-ray crystallography, cryogenic electron microscopy (cryo-EM) and nuclear magnetic resonance (NMR) spectroscopy provide noisy and partial measurements from which the 3D structure of biomolecules can be inferred. This three-dimensional information is key for our understanding of the molecular machinery of living organisms, as well as for designing therapeutic compounds. However, turning experimental observations into reliable 3D structural models is a challenging computational task. For many years, reconstruction algorithms were based on Maximum-A-Posteriori (MAP) estimation and often resorted to hand-crafted priors to compensate for the ill-posedness of the problem. State-of-the-art algorithms for cryo-EM reconstruction [63, 59] are instances of such “white-box” algorithms. These approaches sometimes provide estimates for the uncertainty of their answers but can only leverage explicitly defined regularizers and do not cope well with complex noise sources or missing data.

Recently, supervised-learning approaches have emerged as an alternative to the MAP framework and some of them established a new empirical state of the art for certain tasks, like model building [39]. Typically, these supervised learning methods view the reconstruction problem as a regression task where a mapping between experimental measurements and atomic models needs to be learned. Some of these, like ModelAngelo, can even combine experimental data with sequence information by

*Correspondence to: axlevy@stanford.edu, gordon.wetzstein@stanford.edu

leveraging a pretrained protein language model [60]. However, these methods must be trained on *paired* data (i.e., must be given input–output pairs) and can only cope with a predefined type of input. If additional information is available in a format that the model was not trained on (e.g., structural information about a fragment of the protein), or if the distribution of input data shifts at inference time (e.g., if the noise level changes due to modifications in the experimental protocol), a new model needs to be trained to properly cope with the new data.

In the field of imaging, scenarios where an image or a 3D model must be inferred from corrupted and partial observations are known as “inverse problems”. To overcome the ill-posedness of these problems, regularizers were heuristically defined to inject hand-crafted priors and turn Maximum Likelihood Estimation (MLE) problems into MAP problems. In a similar fashion, machine learning-based methods were recently shown to outperform hand-crafted algorithms for a wide variety of tasks: denoising [86], inpainting [82], super-resolution [49], deblurring [53], monocular depth estimation [27], and camera calibration [42], among others. These methods, however, are equally limited by their need for paired data and their poor performance in the eventuality of a distribution shift.

In contrast, the MAP approach does not require paired data and can leverage the knowledge of the physics behind the problem through the definition of a likelihood function. As for the prior, generative models were shown to be effective tools to inject data-driven priors into MAP problems, making inverse problems well-posed while circumventing the need for heuristic priors [5]. Among these generative methods, diffusion models gained popularity due to their powerful capabilities in the unconditional generation of images [25], videos [34], and 3D assets [57], and were recently leveraged to solve inverse problems in image space [67, 12]. The field of structural biology has also witnessed the application of diffusion models in protein structure modeling tasks [79, 1]. The recently released generative model Chroma [37] stands out in part thanks to its “programmable” framework, i.e., its ability to be conditioned on external hard or soft constraints, but was never applied to structure determination problems like atomic model building.

Here, we introduce ADP-3D (Atomic Denoising Prior for 3D reconstruction), a framework to condition a diffusion model in protein space with any observations for which the measurement process can be physically modeled. Instead of using unadjusted Langevin dynamics for posterior sampling, our approach performs MAP estimation and leverages the data-driven prior learned by a diffusion model using the plug-n-play framework [75], [88]. We demonstrate that our method handles a variety of external information: cryo-EM density maps, amino acid sequence, partial 3D structure, and pairwise distances between amino acid residues, to refine a complete 3D atomic model of the protein. We show that our method outperforms a posterior sampling baseline in average accuracy and, given a cryo-EM density map, can accurately refine incomplete atomic models provided by ModelAngelo. ADP-3D can leverage any protein diffusion model as a prior, which we demonstrate by showing results obtained with Chroma [37] and RFdiffusion [79]. We therefore make the following contributions:

- We introduce a versatile framework, inspired by plug-n-play, to solve inverse problems in protein space with a pretrained diffusion model as a learned prior;
- We outperform an existing posterior sampling method at reconstructing full protein structures from partial structures;
- We show that a protein diffusion model can be guided to perform atomic model refinement in simulated and experimental cryo-EM density maps;
- We show that a protein diffusion model can be conditioned on a sparse distance matrix.

2 Related Work

Protein Diffusion Models. Considerable progress has been made in leveraging diffusion models for protein structure generation. While the first models could sample distance matrices [46], they were later improved to directly sample backbone structures represented by 3D point clouds [2, 74], backbone internal coordinates [81], 3D “frames” [84]. Recent methods are able to directly sample all-atom structures, including side chains [10]. In RFdiffusion, Watson et al. [79] experimentally designed the generated proteins and structurally validated them with cryo-EM. In Chroma, Ingraham et al. [37] introduced a “conditioning” framework to generate proteins with desired properties (e.g.,

substructure motifs, symmetries), but this framework was never used to enable protein structure determination from experimental measurements. Recently, AlphaFold 3 [1] showed that a diffusion model operating on raw atom coordinates could be used as a tool to improve protein structure prediction. As generative models for proteins keep improving, leveraging them in the most impactful way becomes an increasingly important matter.

Here, we introduce a framework to efficiently condition a pretrained protein diffusion model and demonstrate the possibility of using cryo-EM maps as conditioning information. Most of our experiments are conducted using Chroma as a prior and we provide additional results using RFdiffusion in the supplements.

Diffusion-Based Posterior Sampling in Image Space. An *inverse problem* in image space can be defined by $\mathbf{y} = \Gamma(\mathbf{x}) + \eta$ where \mathbf{x} is an unknown image, \mathbf{y} a measurement, Γ a known operator and η a noise vector of known distribution, potentially signal-dependent. The goal of posterior sampling is to sample \mathbf{x} from the posterior $p(\mathbf{x}|\mathbf{y})$, the normalized product of the prior $p(\mathbf{x})$ and the likelihood $p(\mathbf{y}|\mathbf{x})$. Bora et al. [5] showed that generative models could be leveraged to implicitly represent a data-learned prior and solve compressed sensing problems in image space. Motivated by the success of diffusion models at unconditional generation [25], several works showed that score-based and denoising models could be used to solve linear inverse problems like super-resolution, deblurring, inpainting and colorization [47, 9, 62, 41, 51, 88], leading to results of unprecedented quality. Other methods leveraged the score learned by a diffusion model to solve inverse problems in medical imaging [68, 38, 11, 14, 13] and astronomy [69]. Finally, recent methods went beyond the scope of linear problems and used diffusion-based posterior sampling on nonlinear problems like JPEG restoration [67], phase retrieval and non-uniform deblurring [12]. We refer to Daras et al. [19] for an in-depth survey of the methods leveraging diffusion models as priors in inverse problems. Taking inspiration from these methods, and in particular from DiffPIR [88], we propose to leverage protein diffusion models to solve nonlinear inverse problems in protein space.

Model Building Methods. Cryogenic electron-microscopy (cryo-EM) provides an estimate of the 3D electron scattering potential (or density map) of a protein. The task of fitting an atomic model \mathbf{x} into this 3D map \mathbf{y} is called model building and can be seen as a nonlinear inverse problem in protein space (see 4.3).

Model building methods were first developed in X-Ray crystallography [15] and automated methods like Rosetta *de-novo* [76], PHENIX [48, 73] and MAINMAST [72] were later implemented for cryo-EM data. Although they constituted a milestone towards the automation of model building, obtained structures were often incomplete and needed refinement [66]. Supervised learning techniques were applied to model building, relying on U-Net-based architectures [65, 87, 55], or combining a 3D transformer with a Hidden Markov Model [31]. EMBuild [33] was the first method to make use of sequence information and ModelAngelo [39] established a new state of the art for automated *de novo* model building. Trained on 3,715 experimental paired datapoints, ModelAngelo uses a GNN-based architecture and processes the sequence information with a pretrained language model [60]. Although fully-supervised methods outperform previous approaches, they still provide incomplete atomic models and cannot use a type of input data it was not trained with as additional information.

Here, we propose a versatile framework to solve inverse problems in protein space, including atomic model refinement. Our approach can cope with auxiliary measurements for which the measurement process is known. Our framework allows any pretrained diffusion model to be plugged-in as a prior and can therefore take advantage of future developments in generative models without any task-specific retraining step.

3 Background

3.1 Diffusion in Protein Space with Chroma

In Chroma [37], the atomic structure of a protein of N amino acid residues is represented by the 3D Cartesian coordinates $\mathbf{x} \in \mathbb{R}^{4N \times 3}$ of the four backbone heavy atoms (N, C $_{\alpha}$, C, O) in each residue, the amino acid sequence $\mathbf{s} \in \{1, \dots, 20\}^N$, and the side chain torsion angles for each amino acid $\chi \in (-\pi, \pi]^{4N}$ (the conformation of the side chain can be factorized as up to four sequential

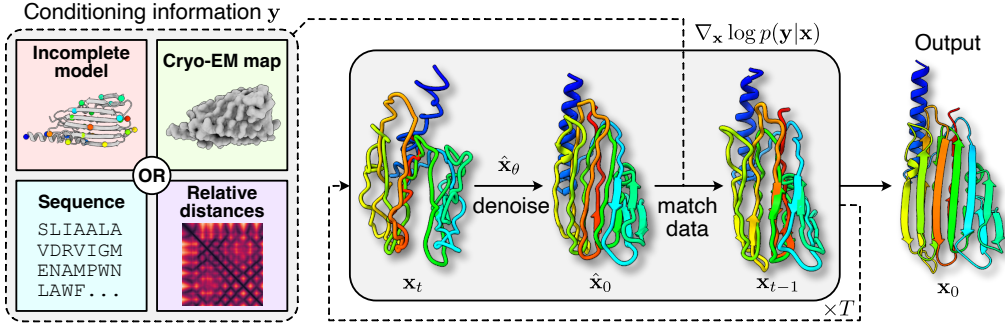


Figure 1: Overview of ADP-3D. Our method turns partial and noisy measurements (the “conditioning information”) into a 3D structure by leveraging a pretrained diffusion model and physics-based models of the measurement processes. Starting from a random structure \mathbf{x}_T , our method iterates between a denoising step and a data-matching step. The denoiser comes from the pretrained diffusion model. The data-matching step aims at maximizing the likelihood of the measurements.

rotations). The joint distribution over all-atom structures is factorized as

$$p(\mathbf{x}, \mathbf{s}, \chi) = p(\mathbf{x})p(\mathbf{s}|\mathbf{x})p(\chi|\mathbf{x}, \mathbf{s}). \quad (1)$$

The first factor on the right hand side, $p(\mathbf{x})$, is modeled as a diffusion process operating in the space of backbone structures \mathbf{x} . Given a structure \mathbf{x} at diffusion time t , Chroma models the conditional distribution of the sequence $p_\theta(\mathbf{s}|\mathbf{x}, t)$ as a conditional random field and the conditional distribution of the side chain conformations $p_\theta(\chi|\mathbf{x}, \mathbf{s}, t)$ with an autoregressive model.

Adding isotropic Gaussian noise to a backbone structure would rapidly destroy simple biophysical patterns that proteins always follow (e.g., the scaling law of the radius of gyration with the number of residues). Instead, Chroma uses a non-isotropic noising process as an inductive bias to alleviate the need for the model to learn these patterns from the data. The correlation of the noise is defined in such a way that a few structural properties are statistically preserved throughout the noising process. Specifically, the forward diffusion process is defined by the variance-preserving stochastic process

$$d\mathbf{x} = -\frac{1}{2}\mathbf{x}\beta_t dt + \sqrt{\beta_t}\mathbf{R}d\mathbf{w}, \quad (2)$$

where β_t is a time-dependent noising schedule and $d\mathbf{w}$ is a standard Wiener process of dimension $\mathbb{R}^{4N \times 3}$. The matrix $\mathbf{R} \in \mathbb{R}^{4N \times 4N}$ is fixed and defined explicitly based on statistical considerations regarding the structure of proteins (see Ingraham et al. [37] and supplements). Starting from \mathbf{x}_0 at $t = 0$, a solution to this stochastic differential equation (SDE) at time t is given by

$$\mathbf{x}_t \sim \mathcal{N}(\mathbf{x}; \alpha_t \mathbf{x}_0, \sigma_t^2 \mathbf{R}\mathbf{R}^T), \quad (3)$$

where $\alpha_t = \exp\left(-\frac{1}{2}\int_0^t \beta_s ds\right)$ and $\sigma_t = \sqrt{1 - \alpha_t^2}$.

New protein samples can be generated by sampling \mathbf{x}_T from $\mathcal{N}(0, \mathbf{R}\mathbf{R}^T)$ and integrating the following reverse-time SDE over $t \in [T, 0]$ [3]:

$$d\mathbf{x} = \left[-\frac{1}{2}\mathbf{x} - \mathbf{R}\mathbf{R}^T \nabla_{\mathbf{x}} \log p_t(\mathbf{x})\right] \beta_t dt + \sqrt{\beta_t}\mathbf{R}d\bar{\mathbf{w}}, \quad (4)$$

where $d\bar{\mathbf{w}}$ is a reverse-time Wiener process. Following Tweedie’s formula [61], the score $\nabla_{\mathbf{x}} \log p_t(\mathbf{x})$ is an affine function of the time-dependent *optimal denoiser*, approximated by $\hat{\mathbf{x}}_\theta(\mathbf{x}, t)$:

$$\nabla_{\mathbf{x}} \log p_t(\mathbf{x}) = \frac{(\mathbf{R}\mathbf{R}^T)^{-1}}{1 - \alpha_t^2} (\alpha_t \mathbb{E}[\mathbf{x}_0|\mathbf{x}_t = \mathbf{x}] - \mathbf{x}), \quad \hat{\mathbf{x}}_\theta(\mathbf{x}, t) \approx \mathbb{E}[\mathbf{x}_0|\mathbf{x}_t = \mathbf{x}]. \quad (5)$$

3.2 Half Quadratic Splitting and Plug-n-Play Framework

An objective function of the form $f(\mathbf{x}) + g(\mathbf{x})$ can be efficiently minimized over \mathbf{x} using a variable splitting algorithm like Half Quadratic Splitting (HQS) [30]. By introducing an auxiliary variable $\tilde{\mathbf{x}}$, the HQS method relies on iteratively solving two subproblems:

$$\begin{aligned} \tilde{\mathbf{x}}_k &= \text{prox}_{g, \gamma}(\mathbf{x}_k) = \underset{\tilde{\mathbf{x}}}{\text{argmin}} \quad g(\tilde{\mathbf{x}}) + \frac{\gamma}{2} \|\tilde{\mathbf{x}} - \mathbf{x}_k\|_2^2, \\ \mathbf{x}_{k+1} &= \text{prox}_{f, \gamma}(\tilde{\mathbf{x}}_k) = \underset{\mathbf{x}}{\text{argmin}} \quad f(\mathbf{x}) + \frac{\gamma}{2} \|\mathbf{x} - \tilde{\mathbf{x}}_k\|_2^2, \end{aligned} \quad (6)$$

where prox are called “proximal operators” and $\gamma > 0$ is a user-defined proximal parameter.

If f represents a negative log-likelihood over \mathbf{x} and g represents a negative log-prior, the above problem defines a Maximum-A-Posterior (MAP) problem. The key idea of the plug-and-play framework [75] is to notice that the first minimization problem in (6) is exactly a Gaussian denoising problem at noise level $\sigma = \sqrt{1/\gamma}$ with the prior $\exp(-g(\mathbf{x}))$ in \mathbf{x} -space. This means that any Gaussian denoiser can be used to “plug in” a prior into a MAP problem.

Once a diffusion model has been trained, it provides a deterministic Gaussian denoiser for various noise levels, as described in (5). As recently shown in Zhu et al. [88], this optimal denoiser can be used in the plug-n-play framework to solve MAP problems in image space. Here, we propose to apply this idea to inverse problems in protein space, leveraging a pretrained diffusion model.

4 Methods

In this section, we formulate our method, ADP-3D (Atomic Denoising Prior for 3D reconstruction), as a MAP estimation method in protein space and explain how the plug-n-play framework can be used to leverage the prior learned by a pretrained diffusion model. The method is described visually in Figure 1. We then introduce our preconditioning strategy in the case of linear problems. Finally, we describe and model the measurement process in cryogenic electron microscopy. ADP-3D is described with pseudo-code in Algorithm 1.

4.1 General Approach

Given a set of independent measurements $\mathbf{Y} = \{\mathbf{y}_i\}_{i=1}^n$ made from the same unknown protein, our goal is to find a Maximum-A-Posteriori (MAP) estimate of the backbone structure \mathbf{x}^* . Following Bayes’ rule,

$$\mathbf{x}^* = \underset{\mathbf{x}}{\operatorname{argmax}} \{p_0(\mathbf{x}|\mathbf{Y})\} = \underset{\mathbf{x}}{\operatorname{argmin}} \left\{ \underbrace{-\sum_{i=1}^n \log p_0(\mathbf{y}_i|\mathbf{x})}_{f(\mathbf{x})} - \underbrace{\log p_0(\mathbf{x})}_{g(\mathbf{x})} \right\}. \quad (7)$$

While most of previous works leveraging a diffusion model for inverse problems aim at sampling from the posterior distribution $p(\mathbf{x}|\mathbf{Y})$, we are interested here in scenarios where the measurements convey enough information to make the MAP estimate unique and well-defined.

We take inspiration from the plug-and-play framework [75] to efficiently solve (7). We propose to use the optimal denoiser $\hat{\mathbf{x}}_\theta(\mathbf{x}, t)$ of a pretrained diffusion model to solve the first subproblem in (6). Framing the optimization loop in the whitened space of $\mathbf{z} = \mathbf{R}^{-1}\mathbf{x}$, which provides more stable results, our general optimization algorithm can be summarized in three steps:

$$\begin{aligned} \tilde{\mathbf{z}}_0 &= \mathbf{R}^{-1}\hat{\mathbf{x}}_\theta(\mathbf{R}\mathbf{z}_t, t) && \text{Denoise at level } t, \\ \hat{\mathbf{z}}_0 &= \underset{\mathbf{z}}{\operatorname{argmin}} \frac{\gamma}{2}\|\mathbf{z} - \tilde{\mathbf{z}}_0\|_2^2 - \sum_{i=1}^n \log p_0(\mathbf{y}_i|\mathbf{z}) && \text{Maximize likelihood,} \\ \mathbf{z}_{t-1} &\sim \mathcal{N}(\alpha_{t-1}\hat{\mathbf{z}}_0, \sigma_{t-1}^2) && \text{Add noise at level } t-1. \end{aligned}$$

Here, no specific assumptions have been made on the likelihood term and this framework could hypothetically be applied on any set of measurements for which we have a physics-based model of the measurement process. Since the second step is not tractable in most cases, we replace the explicit minimization with a gradient step with momentum from the iterate $\tilde{\mathbf{z}}_0$. This step can be implemented efficiently using automatic differentiation. The gradient of $\|\mathbf{z} - \hat{\mathbf{z}}_0\|_2^2$ w.r.t \mathbf{z} in $\hat{\mathbf{z}}_0$ being null, the method does not depend on the choice γ .

4.2 Preconditioning for Linear Measurements

We consider the case where the measurement process is linear:

$$\mathbf{y} = \mathbf{A}\mathbf{x}_0 + \eta = \mathbf{A}\mathbf{R}\mathbf{z}_0 + \eta, \quad \eta \sim \mathcal{N}(0, \boldsymbol{\Sigma} \in \mathbb{R}^{m \times m}), \quad (8)$$

Algorithm 1 ADP-3D (Atomic Denoising Prior for 3D reconstruction)

Inputs: log-likelihood functions $\{f_i : (\mathbf{y}, \mathbf{z}) \mapsto \log p(\mathbf{y}_i = \mathbf{y} | \mathbf{z})\}_{i=1}^n$, measurements $\{\mathbf{y}_i\}$.
Diffusion model: correlation matrix \mathbf{R} , denoiser $\hat{\mathbf{x}}_\theta(\mathbf{x}, t)$, schedule $\{\alpha_t, \sigma_t\}_{t=1}^T$.
Optimization parameters: learning rates $\{\lambda_i\}$, momenta $\{\rho_i\}$.
Initialization: $\mathbf{z}_T \leftarrow \mathcal{N}(0, \mathbf{I})$, $\forall i, \mathbf{v}_i = 0$
for $t = T, \dots, 1$ **do**
 $\tilde{\mathbf{z}}_0 \leftarrow \mathbf{R}^{-1} \hat{\mathbf{x}}_\theta(\mathbf{R}\mathbf{z}_t, t)$ Denoise at level t
 $\forall i, \mathbf{v}_i = \rho_i \mathbf{v}_i + \lambda_i \nabla_{\mathbf{z}} f_i(\mathbf{y}_i, \mathbf{z})|_{\mathbf{z}=\tilde{\mathbf{z}}_0}$ Accumulate gradient of log-likelihood
 $\hat{\mathbf{z}}_0 \leftarrow \tilde{\mathbf{z}}_0 + \sum_i \mathbf{v}_i$ Take a step to maximize likelihood
 $\mathbf{z}_{t-1} \sim \mathcal{N}(\alpha_{t-1} \hat{\mathbf{z}}_0, \sigma_{t-1}^2)$ Add noise at level $t - 1$
end for
return $\mathbf{x}_0 = \mathbf{R}\mathbf{z}_0$

with $\mathbf{y} \in \mathbb{R}^m$ and $\mathbf{A} \in \mathbb{R}^{m \times 4N}$ being a known measurement matrix of rank m . In this case, the log-likelihood term is a quadratic function:

$$\log p_0(\mathbf{y} | \mathbf{z}) = -\frac{1}{2} \|\mathbf{A}\mathbf{R}\mathbf{z} - \mathbf{y}\|_{\Sigma^{-1}}^2 + C, \text{ where } \|\mathbf{x}\|_{\Sigma^{-1}}^2 = \mathbf{x}^T \Sigma^{-1} \mathbf{x}, \quad (9)$$

and C does not depend on \mathbf{z} . As shown in the supplements, the condition number of \mathbf{R} (i.e., the ratio between its largest and smallest singular values) grows as a power function of the number of residues. For typical proteins ($N \geq 100$), this condition number exceeds 100, making the maximization of the above term an ill-conditioned problem. In order to make gradient-based optimization more efficient, we propose to *precondition* the problem by precomputing a singular value decomposition $\mathbf{A}\mathbf{R} = \mathbf{U}\mathbf{S}\mathbf{V}^T$ and to set $\Sigma = \sigma^2 \mathbf{U}\mathbf{S}\mathbf{S}^T \mathbf{U}^T$. Note that this is equivalent to modeling the measurement process as $\mathbf{y} = \mathbf{A}\mathbf{R}(\mathbf{z} + \tilde{\eta})$ with $\tilde{\eta} \sim \mathcal{N}(0, \sigma^2)$. In other words, we assume that the noise η preserves the simple patterns in proteins, which is a reasonable hypothesis if, for example, \mathbf{y} is an incomplete atomic model obtained by an upstream reconstruction algorithm that leverages prior knowledge on protein structures. The log-likelihood then becomes

$$\log p_0(\mathbf{y} | \mathbf{z}) = -\frac{1}{2\sigma^2} \left\| \begin{pmatrix} \mathbf{I}_m & 0 \\ 0 & 0 \end{pmatrix} \mathbf{V}^T \mathbf{z} - \mathbf{S}^+ \mathbf{U}^T \mathbf{y} \right\|_2^2 + C. \quad (10)$$

The maximization of this term is a well-posed problem that gradient ascent with momentum efficiently solves (see supplementary analyses). In (10), \mathbf{S}^+ denotes the pseudo-inverse of \mathbf{S} .

4.3 Application to Atomic Model Building

Measurement Model in Cryo-EM. In single particle cryo-EM, a purified solution of a target protein is flash-frozen and imaged with a transmission electron microscope, providing thousands to millions of randomly oriented 2D projection images of the protein’s electron scattering potential. Reconstruction algorithms process these images and infer a 3D *density map* of the protein. Given a protein $(\mathbf{x}, \mathbf{s}, \chi)$, its density map is well approximated by [22]

$$\mathbf{y} = \mathcal{B}(\Gamma(\mathbf{x}, \mathbf{s}, \chi)) + \eta \in \mathbb{R}^{D \times D \times D}, \quad (11)$$

where Γ is an operator that places a sum of 5 isotropic Gaussians centered on each heavy atom. The amplitudes and standard deviations of these Gaussians, known as “form factors”, are tabulated [32] and depend on the chemical element they are centered on. \mathcal{B} represents the effect of “B-factors” [40] and can be viewed as a spatially dependent blurring kernel modelling molecular motions and/or signal damping by the transfer function of the electron microscope. η models isotropic Gaussian noise of variance σ^2 . This measurement model leads to the following log-likelihood:

$$\log p_0(\mathbf{y} | \mathbf{x}, \mathbf{s}, \chi) = -\frac{1}{2\sigma^2} \|\mathbf{y} - \mathcal{B}(\Gamma(\mathbf{x}, \mathbf{s}, \chi))\|_2^2 + C. \quad (12)$$

Likelihood Terms in Model Refinement. We consider a 3D density map \mathbf{y} provided by an upstream reconstruction method and an incomplete backbone structure $\bar{\mathbf{x}} \in \mathbb{R}^m$ ($m \leq 4N$) provided by an upstream model building algorithm (e.g., ModelAngelo [39]). Sequencing a protein is now a routine process [23] and we therefore consider the sequence \mathbf{s} as an additional source of information. The side chain angles χ are, however, unknown.

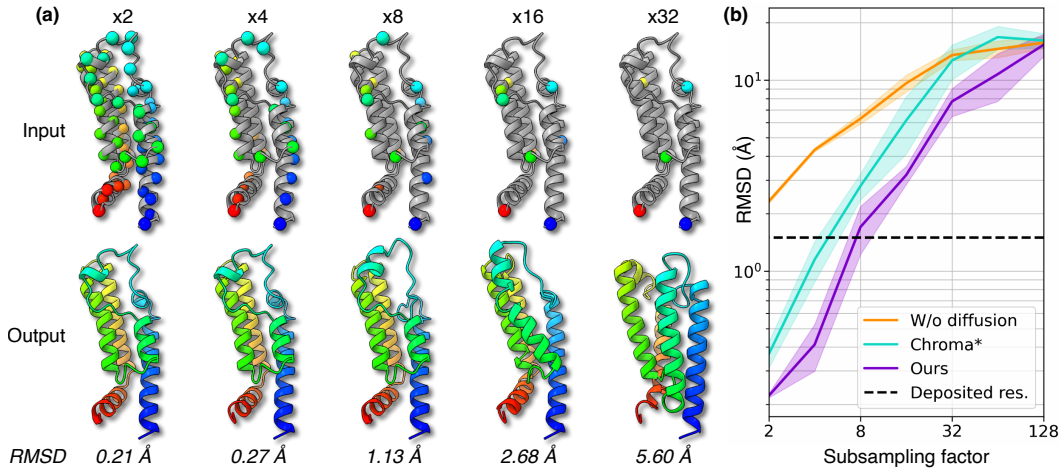


Figure 2: Structure Completion. Results on the ATAD2 protein (PDB: 7qum, 130 residues). (a) Qualitative results. The input structure is a subsampled version of the target structure (subsampling factor in the top row). In the “input” row, we show the target (unknown) in gray and the locations of the known alpha carbons in colors. We report the lowest RMSD over 8 runs. (b) RMSD vs. subsampling factor. Our method is compared to Chroma conditioned with the `SubstructureConditioner`. The importance of the diffusion-based prior is shown. We report the mean RMSD (± 1 std) over 8 runs. The experimental (deposited) resolution is indicated with a dashed line.

The log-likelihood of our measurements for a given backbone structure \mathbf{x} can be decomposed as

$$\log p_0(\mathbf{y}, \mathbf{s}, \bar{\mathbf{x}}|\mathbf{x}) = \log p_0(\bar{\mathbf{x}}|\mathbf{x}) + p_0(\mathbf{y}, \mathbf{s}|\mathbf{x}) = \log p_0(\bar{\mathbf{x}}|\mathbf{x}) + \log p_0(\mathbf{y}|\mathbf{x}, \mathbf{s}) + \log p_0(\mathbf{s}|\mathbf{x}). \quad (13)$$

On the right-hand side, the last term can be approximated using the learned conditional distribution $p_\theta(\mathbf{s}|\mathbf{x})$. We model $\bar{\mathbf{x}} = \mathbf{M}\mathbf{x} + \boldsymbol{\eta}$ so that the first term can be handled by the preconditioning procedure described in the previous section. Finally, the middle term involves the marginalization of $p_0(\mathbf{y}|\mathbf{x}, \mathbf{s}, \chi)$ over χ . This marginalization is not tractable but (12) provides a lower bound:

$$\log p_0(\mathbf{y}|\mathbf{x}, \mathbf{s}) \geq \mathbb{E}_{\chi \sim p_0(\chi|\mathbf{x}, \mathbf{s})} [\log p_0(\mathbf{y}|\mathbf{x}, \mathbf{s}, \chi)] \approx \mathbb{E}_{\chi \sim p_\theta(\chi|\mathbf{x}, \mathbf{s})} [\log p_0(\mathbf{y}|\mathbf{x}, \mathbf{s}, \chi)], \quad (14)$$

using Jensen’s inequality. The expectation is approximated by Monte Carlo sampling and gradients of χ with respect to \mathbf{x} are computed by automatic differentiation through the autoregressive sampler of χ , following the “reparameterization trick” [43].

5 Experiments

Experimental Setup. Our main results are obtained using the publicly released version of Chroma² [37]. We provide additional results with the publicly released version of RFdiffusion³ [79] in the supplements. We run all our experiments using structures of proteins downloaded from the Protein Data Bank (PDB) [6]. In order to select proteins that do not belong to the training dataset of Chroma, here we only consider structures that were released after 2022-03-20 (Chroma was trained on a filtered version of the PDB queried on that date). We provide additional results on structures taken from the CASP15 dataset in the supplements. For the proteins that are not fully modeled on the PDB, we mask out the residues with ground truth coordinates before computing the Root Mean Square Deviation (RMSD). In each experiment, we run 8 replicas in parallel on a single NVIDIA A100 GPU. Further details about each target structure are provided in the supplements.

Structure Completion. Given an incomplete atomic model of a protein, our first task is to predict the coordinates of all heavy atoms in the backbone. This first task is designed as a toy problem, with no immediate application to real data, to validate and evaluate our method. The forward measurement process can be modeled as $\mathbf{y} = \mathbf{M}\mathbf{x}$ where $\mathbf{M} \in \{0, 1\}^{(4N/k) \times 4N}$ is a *masking matrix* ($\mathbf{M}\mathbf{1} = \mathbf{1}$) and k is the *subsampling factor*. We consider the case where, for each residue, the location of all 4 heavy atoms on the backbone (N, C $_{\alpha}$, C, O) is either known or unknown. Residues of known locations are regularly spaced along the backbone every k residues. We compare our results to the baseline Chroma conditioned with a `SubstructureConditioner` [37]. This baseline samples from

²<https://github.com/generatebio/chroma>

³<https://github.com/RosettaCommons/RFdiffusion>

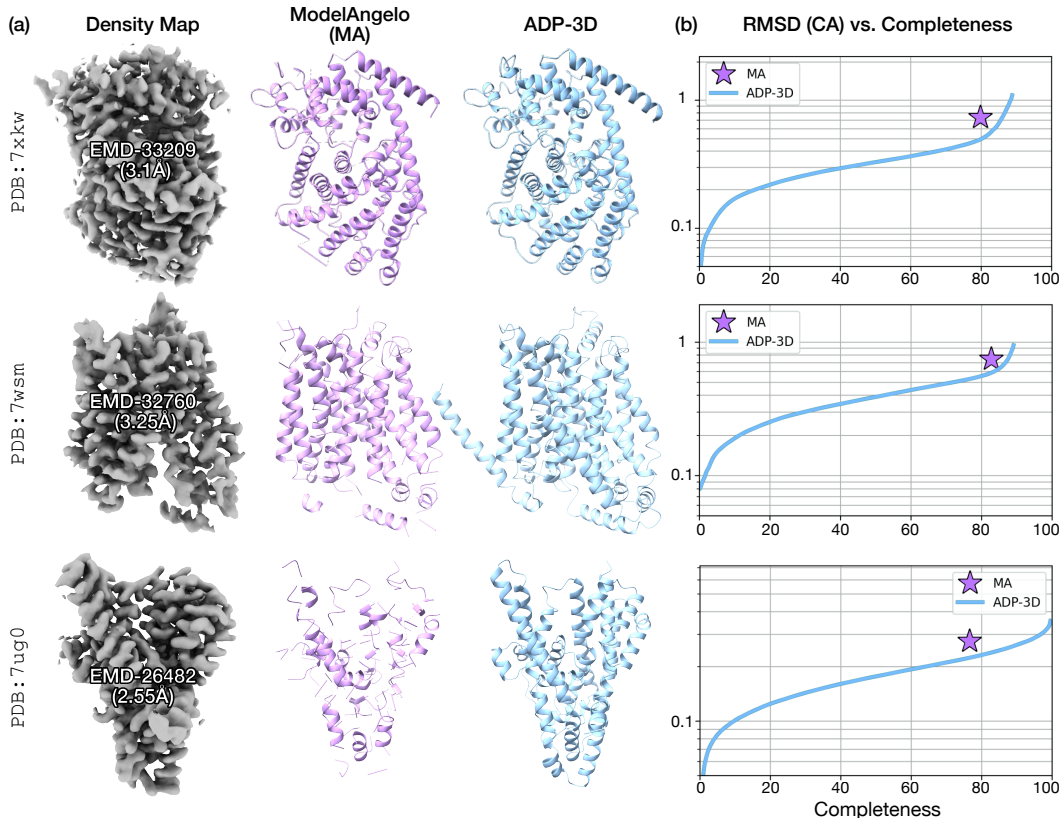


Figure 3: Atomic Model Refinement. (a) Experimental density map, ModelAngelo’s incomplete model and ADP-3D’s atomic model. (b) RMSD of alpha carbons vs. completeness (number of predicted residues / total number of residues) with ModelAngelo (MA) and our method. For EMD-26482 (third row), we remove uniformly sampled residues from the ModelAngelo model until reaching sub-80% of completeness. The RMSD is computed with respect to the deposited structure on the PDB.

the posterior probability $p(x|y)$ using unadjusted Langevin dynamics. We use 1000 diffusion steps for our method and the baseline.

In Figure 2, we show our results on ATAD2 (PDB: 7qum) [21, 4], a cancer-associated protein of 130 residues. The protein was resolved at a resolution of 1.5 Å using X-ray crystallography. Our method recovers the target structure without loss of information (RMSD < 1.5 Å) for subsampling factors of 2, 4 and 8. Fig. 2.b shows that our method outperforms the baseline and highlights the importance of the diffusion-based prior. When the subsampling factor is large (≥ 32), the reconstruction accuracy decreases but the method inpaints unknown regions with realistic secondary structures (see quantitative evaluation in the supplementary). Note that making the conditioning information sparser (increasing the subsampling factor) tends to close the gap between our method (MAP estimation) and the baseline (posterior sampling).

Atomic Model Refinement. Next, we evaluate our method on the model refinement task. We use experimental cryo-EM maps of single-chain structures: EMD-33209 (density map of PDB: 7xkw [83]), EMD-32760 (density map of PDB: 7wsm [85]), EMD-26482 (density map of PDB: 7ug0 [36]). We directly use the publicly available versions of EMD-33209 and EMD-32760, and run ModelAngelo [39] with its default parameters. For EMD-26482, the deposited map is a trimeric version of PDB: 7ug0. We use the `volume zone` tool of ChimeraX to select and keep the regions of the density map within 3 Å of the deposited atomic model. We then run ModelAngelo using its default parameters. All the incomplete models provided by ModelAngelo are cleaned by removing the residues for which the $C\alpha$ atom is not located within 3.8 ± 0.3 Å of both neighboring $C\alpha$ atoms. For the model obtained from EMD-26482, we also randomly remove uniformly sampled residues in the incomplete model, such that the completeness gets below 80%. We provide ModelAngelo’s output (an incomplete model) to our method, along with the density map and the sequence. To evaluate our method, we report the

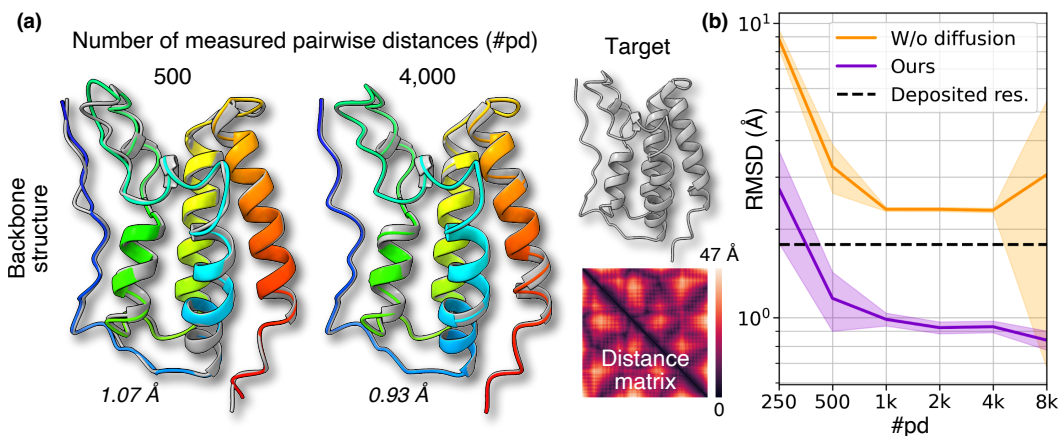


Figure 4: Pairwise Distances to Structures. Results on BRD4 (PDB: 7r5b, 127 residues) (a) Qualitative results. The reconstructed structures are shown in colors, depending on the number of known pairwise distances. We report the lowest RMSD over 8 runs. The target structure is shown in gray along with its pairwise distance matrix. (b) RMSD vs. number of known pairwise distances. Each experiment is ran 10 times with randomly sampled distances. We report the mean of the lowest RMSD obtained over 8 replicas (± 1 std). The plot demonstrates the importance of the diffusion model. The experimental (deposited) resolution is indicated with a dashed line.

RMSD of the predicted structure for the $X\%$ most well-resolved alpha carbons (compared to the deposited structure), for $X \in [0, 100]$ (X is called the “completeness”).

We show qualitative and quantitative results in Figure 3. For all structures, ADP-3D improves the accuracy of the ModelAngelo model for the same level of completeness. Note that the RMSD can only be computed up to the completeness level of the deposited structure. We provide additional results in the supplements and investigate on the influence of the resolution of the input density map and we perform an ablation study on the conditioning information.

Pairwise Distances to Structure Finally, we assume we are given a set of pairwise distances between alpha carbons and we use our method to predict a full 3D structure. This task is a simplification of the reconstruction problem in paramagnetic NMR spectroscopy, where one can obtain information about the relative distances and orientations between pairs of atoms via the nuclear Overhauser effect and sparse paramagnetic restraints, and must deduce the Cartesian coordinates of every atom [44, 45], [64, 80, 54]. Formally, our measurement model is $\mathbf{y} = \|\mathbf{D}\mathbf{x}\|_2 \in \mathbb{R}^m$, where $\mathbf{D} \in \{-1, 0, 1\}^{m \times 4N}$ is the *distance matrix* and the norm is taken row-wise (in xyz space). \mathbf{D} contains a single “1” and a single “-1” in each row and is not redundant (the distance between a given pair of atoms is measured at most once). m corresponds to the number of measured distances.

We evaluate our method on the bromodomain-containing protein 4 (BRD4, PDB: 7r5b [78]), a protein involved in the development of a specific type of cancer (NUT midline carcinoma) [28] and targeted by pharmaceutical drugs [18]. For a given number m , we randomly sample m pairs of alpha carbons (without redundancy) between which we assume the distances to be known. Our results are shown in Figure 4. When 500 pairwise distances or more are known, our method recovers the structural information of the target structure (RMSD < 1.77 Å, the resolution of the deposited structure resolved with X-ray crystallography). We conduct the same experiment without the diffusion model and show a drop of accuracy, highlighting the importance of the generative prior. Note that, when the diffusion model is removed, increasing the number of measurements increases the number of local minima in the objective function and can therefore hurt the reconstruction quality (plot in Fig. 4, orange curve, far-right part).

6 Discussion

This paper introduces ADP-3D, a method to leverage a pretrained protein diffusion model for protein structure determination. ADP-3D is not tied to a specific diffusion model and allows for any data-driven denoisers to be plugged in as priors. Our method can therefore continually benefit from the development of more powerful or more specialized generative models.

Considering real data (e.g., cryo-EM, X-ray crystallography or NMR data) raises complex and exciting challenges, as experimental measurements of any one specific task typically require a lot of domain-specific processing. For example, in a real scenario, NMR experiments cannot probe long

pairwise distances above 6 Å. Taking these constraints into account and applying ADP-3D to real NMR data would be an exciting direction for future work. In cryo-EM, most of the analyzed proteins are multi-chain while the current implementation of ADP-3D only supports single-chain structures. Extending our framework to multi-chain structures, which would be possible using diffusion models like Chroma, would be an impactful future direction.

In cases where the measurement process cannot be faithfully modeled due to complex nonidealities, or when the measurement process is not differentiable, our framework reaches its boundaries. Exploring the possibility of finetuning a pretrained diffusion model on paired data for conditional generation constitutes another promising avenue for future work.

Acknowledgment

The author(s) are pleased to acknowledge that the work reported on in this paper was substantially performed using the Princeton Research Computing resources at Princeton University which is a consortium of groups led by the Princeton Institute for Computational Science and Engineering (PICSciE) and Office of Information Technology’s Research Computing. The Zhong lab gratefully acknowledges support from the Princeton Catalysis Initiative, Princeton School of Engineering and Applied Sciences, and Generate Biomedicines. The funders had no role in study design, data collection and analysis, decision to publish or preparation of the manuscript.

Code Availability

Our code is publicly available at: <https://github.com/axel-levy/axlevy-adp-3d>

References

- [1] Josh Abramson, Jonas Adler, Jack Dunger, Richard Evans, Tim Green, Alexander Pritzel, Olaf Ronneberger, Lindsay Willmore, Andrew J Ballard, Joshua Babrick, et al. Accurate structure prediction of biomolecular interactions with alphafold 3. *Nature*, pages 1–3, 2024.
- [2] Namrata Anand and Tudor Achim. Protein structure and sequence generation with equivariant denoising diffusion probabilistic models. *arXiv preprint arXiv:2205.15019*, 2022.
- [3] Brian DO Anderson. Reverse-time diffusion equation models. *Stochastic Processes and their Applications*, 12(3):313–326, 1982.
- [4] Paul Bamborough, Chun-wa Chung, Emmanuel H Demont, Rebecca C Furze, Andrew J Bannister, Ka Hing Che, Hawa Diallo, Clement Douault, Paola Grandi, Tony Kouzarides, et al. A chemical probe for the atad2 bromodomain. *Angewandte Chemie*, 128(38):11554–11558, 2016.
- [5] Ashish Bora, Ajil Jalal, Eric Price, and Alexandros G Dimakis. Compressed sensing using generative models. In *International conference on machine learning*, pages 537–546. PMLR, 2017.
- [6] Stephen K Burley, Charmi Bhikadiya, Chunxiao Bi, Sebastian Bittrich, Li Chen, Gregg V Crichlow, Cole H Christie, Kenneth Dalenberg, Luigi Di Costanzo, Jose M Duarte, et al. Rcsb protein data bank: powerful new tools for exploring 3d structures of biological macromolecules for basic and applied research and education in fundamental biology, biomedicine, biotechnology, bioengineering and energy sciences. *Nucleic acids research*, 49(D1):D437–D451, 2021.
- [7] Simon G Caulton, Carey Lambert, Jess Tyson, Paul Radford, Asmaa Al-Bayati, Samuel Greenwood, Emma J Banks, Callum Clark, Rob Till, Elisabete Pires, et al. *Bdellovibrio bacteriovorus* uses chimeric fibre proteins to recognize and invade a broad range of bacterial hosts. *Nature Microbiology*, 9(1):214–227, 2024.
- [8] Anastasiia Chaban, Leonid Minakhin, Ekaterina Goldobina, Brain Bae, Yue Hao, Sergei Borukhov, Leena Putzeys, Maarten Boon, Florian Kabinger, Rob Lavigne, et al. Tail-tape-fused

- virion and non-virion rna polymerases of a thermophilic virus with an extremely long tail. *Nature communications*, 15(1):317, 2024.
- [9] Jooyoung Choi, Sungwon Kim, Yonghyun Jeong, Youngjune Gwon, and Sungroh Yoon. Ilvr: Conditioning method for denoising diffusion probabilistic models. *arXiv preprint arXiv:2108.02938*, 2021.
- [10] Alexander E Chu, Jinho Kim, Lucy Cheng, Gina El Nesr, Minkai Xu, Richard W Shuai, and Po-Ssu Huang. An all-atom protein generative model. *Proceedings of the National Academy of Sciences*, 121(27):e2311500121, 2024.
- [11] Hyungjin Chung and Jong Chul Ye. Score-based diffusion models for accelerated mri. *Medical image analysis*, 80:102479, 2022.
- [12] Hyungjin Chung, Jeongsol Kim, Michael T Mccann, Marc L Klasky, and Jong Chul Ye. Diffusion posterior sampling for general noisy inverse problems. *arXiv preprint arXiv:2209.14687*, 2022.
- [13] Hyungjin Chung, Byeongsu Sim, Dohoon Ryu, and Jong Chul Ye. Improving diffusion models for inverse problems using manifold constraints. *Advances in Neural Information Processing Systems*, 35:25683–25696, 2022.
- [14] Hyungjin Chung, Byeongsu Sim, and Jong Chul Ye. Come-closer-diffuse-faster: Accelerating conditional diffusion models for inverse problems through stochastic contraction. In *Proceedings of the IEEE/CVF Conference on Computer Vision and Pattern Recognition*, pages 12413–12422, 2022.
- [15] Kevin Cowtan. The buccaneer software for automated model building. 1. tracing protein chains. *Acta crystallographica section D: biological crystallography*, 62(9):1002–1011, 2006.
- [16] Melissa R Cruz, Shane Cristy, Shantanu Guha, Giuseppe Buda De Cesare, Elena Evdokimova, Hiram Sanchez, Dominika Borek, Pedro Miramón, Junko Yano, Paul L Fidel Jr, et al. Structural and functional analysis of entv reveals a 12 amino acid fragment protective against fungal infections. *Nature communications*, 13(1):6047, 2022.
- [17] Bonnie J Cuthbert, Jessica Mendoza, Rodger de Miranda, Kadamba Papavinasundaram, Christopher M Sasseti, and Celia W Goulding. The structure of mycobacterium thermoresistibile mmps5 reveals a conserved disulfide bond across mycobacteria. *Metallomics*, 16(3):mfae011, 2024.
- [18] David Da Costa, Angelo Agathangelou, Timothy Perry, Victoria Weston, Eva Petermann, Anastasia Zlatanou, Ceri Oldreive, Wenbin Wei, Grant Stewart, Joanna Longman, et al. Bet inhibition as a single or combined therapeutic approach in primary paediatric b-precursor acute lymphoblastic leukaemia. *Blood cancer journal*, 3(7):e126–e126, 2013.
- [19] Giannis Daras, Hyungjin Chung, Chieh-Hsin Lai, Yuki Mitsufuji, Jong Chul Ye, Peyman Milanfar, Alexandros G Dimakis, and Mauricio Delbracio. A survey on diffusion models for inverse problems. *arXiv preprint arXiv:2410.00083*, 2024.
- [20] Gemma Davison, Mathew P Martin, Shannon Turberville, Selma Dormen, Richard Heath, Amy B Heptinstall, Marie Lawson, Duncan C Miller, Yi Min Ng, James N Sanderson, et al. Mapping ligand interactions of bromodomains brd4 and atad2 with fraglites and peplites-halogenated probes of druglike and peptide-like molecular interactions. *Journal of Medicinal Chemistry*, 65(22):15416–15432, 2022.
- [21] Gemma Davison, Mathew P Martin, Shannon Turberville, Selma Dormen, Richard Heath, Amy B Heptinstall, Marie Lawson, Duncan C Miller, Yi Min Ng, James N Sanderson, et al. Mapping ligand interactions of bromodomains brd4 and atad2 with fraglites and peplites-halogenated probes of druglike and peptide-like molecular interactions. *Journal of Medicinal Chemistry*, 65(22):15416–15432, 2022.
- [22] Marc De Graef. *Introduction to conventional transmission electron microscopy*. Cambridge university press, 2003.

- [23] Edmond De Hoffmann and Vincent Stroobant. *Mass spectrometry: principles and applications*. John Wiley & Sons, 2007.
- [24] Simone A De Rose, Michail N Isupov, Harley L Worthy, Christina Stracke, Nicholas J Harmer, Bettina Siebers, Jennifer A Littlechild, HotSolute consortium, Bettina Siebers, Christopher Bräsen, et al. Structural characterization of a novel cyclic 2, 3-diphosphoglycerate synthetase involved in extremolyte production in the archaeon methanothermus fervidus. *Frontiers in Microbiology*, 14:1267570, 2023.
- [25] Prafulla Dhariwal and Alexander Nichol. Diffusion models beat gans on image synthesis. *Advances in neural information processing systems*, 34:8780–8794, 2021.
- [26] Evelien Dierick, Chana Callens, Yehudi Bloch, Savvas N Savvides, Sarah Hark, Stefan Pelzer, Richard Ducatelle, Filip Van Immerseel, and Evy Goossens. Clostridium perfringens chitinases, key enzymes during early stages of necrotic enteritis in broiler chickens. *PLoS pathogens*, 20(9):e1012560, 2024.
- [27] David Eigen, Christian Puhersch, and Rob Fergus. Depth map prediction from a single image using a multi-scale deep network. *Advances in neural information processing systems*, 27, 2014.
- [28] Christopher A French. Demystified molecular pathology of nut midline carcinomas. *Journal of clinical pathology*, 63(6):492–496, 2010.
- [29] Lavinia Gambelli, Mathew McLaren, Rebecca Connors, Kelly Sanders, Matthew C Gaines, Lewis Clark, Vicki AM Gold, Daniel Kattnig, Mateusz Sikora, Cyril Hanus, et al. Structure of the two-component s-layer of the archaeon sulfolobus acidocaldarius. *Elife*, 13:e84617, 2024.
- [30] Donald Geman and Chengda Yang. Nonlinear image recovery with half-quadratic regularization. *IEEE transactions on Image Processing*, 4(7):932–946, 1995.
- [31] Nabin Giri and Jianlin Cheng. De novo atomic protein structure modeling for cryoem density maps using 3d transformer and hmm. *Nature Communications*, 15(1):5511, 2024.
- [32] Theo Hahn, Uri Shmueli, and JC Wilson Arthur. *International tables for crystallography*, volume 1. Reidel Dordrecht, 1983.
- [33] Jiahua He, Peicong Lin, Ji Chen, Hong Cao, and Sheng-You Huang. Model building of protein complexes from intermediate-resolution cryo-em maps with deep learning-guided automatic assembly. *Nature Communications*, 13(1):4066, 2022.
- [34] Jonathan Ho, William Chan, Chitwan Saharia, Jay Whang, Ruiqi Gao, Alexey Gritsenko, Diederik P Kingma, Ben Poole, Mohammad Norouzi, David J Fleet, et al. Imagen video: High definition video generation with diffusion models. *arXiv preprint arXiv:2210.02303*, 2022.
- [35] Liu Hong and Jinzhi Lei. Scaling law for the radius of gyration of proteins and its dependence on hydrophobicity. *Journal of Polymer Science Part B: Polymer Physics*, 47(2):207–214, 2009.
- [36] Yun Huang, Krishna D Reddy, Clay Bracken, Biao Qiu, Wenhui Zhan, David Eliezer, and Olga Boudker. Environmentally ultrasensitive fluorine probe to resolve protein conformational ensembles by 19f nmr and cryo-em. *Journal of the American Chemical Society*, 145(15): 8583–8592, 2023.
- [37] John B Ingraham, Max Baranov, Zak Costello, Karl W Barber, Wujie Wang, Ahmed Ismail, Vincent Frappier, Dana M Lord, Christopher Ng-Thow-Hing, Erik R Van Vlack, et al. Illuminating protein space with a programmable generative model. *Nature*, 623(7989):1070–1078, 2023.
- [38] Ajil Jalal, Marius Arvinte, Giannis Daras, Eric Price, Alexandros G Dimakis, and Jon Tamir. Robust compressed sensing mri with deep generative priors. *Advances in Neural Information Processing Systems*, 34:14938–14954, 2021.
- [39] Kiarash Jamali, Lukas Käll, Rui Zhang, Alan Brown, Dari Kimanius, and Sjors HW Scheres. Automated model building and protein identification in cryo-em maps. *Nature*, pages 1–2, 2024.

- [40] Satinder Kaur, Josue Gomez-Blanco, Ahmad AZ Khalifa, Swathi Adinarayanan, Ruben Sanchez-Garcia, Daniel Wrapp, Jason S McLellan, Khanh Huy Bui, and Javier Vargas. Local computational methods to improve the interpretability and analysis of cryo-em maps. *Nature communications*, 12(1):1240, 2021.
- [41] Bahjat Kawar, Michael Elad, Stefano Ermon, and Jiaming Song. Denoising diffusion restoration models. *Advances in Neural Information Processing Systems*, 35:23593–23606, 2022.
- [42] Alex Kendall, Matthew Grimes, and Roberto Cipolla. Posenet: A convolutional network for real-time 6-dof camera relocalization. In *Proceedings of the IEEE international conference on computer vision*, pages 2938–2946, 2015.
- [43] Diederik P Kingma. Auto-encoding variational bayes. *arXiv preprint arXiv:1312.6114*, 2013.
- [44] Julia Koehler and Jens Meiler. Expanding the utility of nmr restraints with paramagnetic compounds: background and practical aspects. *Progress in nuclear magnetic resonance spectroscopy*, 59(4):360–389, 2011.
- [45] Georg Kuenze, Richard Bonneau, Julia Koehler Leman, and Jens Meiler. Integrative protein modeling in rosettanmr from sparse paramagnetic restraints. *Structure*, 27(11):1721–1734, 2019.
- [46] Jin Sub Lee, Jisun Kim, and Philip M Kim. Proteinsgm: Score-based generative modeling for de novo protein design. *bioRxiv*, pages 2022–07, 2022.
- [47] Haoying Li, Yifan Yang, Meng Chang, Shiqi Chen, Huajun Feng, Zhihai Xu, Qi Li, and Yueting Chen. Srdiff: Single image super-resolution with diffusion probabilistic models. *Neurocomputing*, 479:47–59, 2022.
- [48] Dorothee Liebschner, Pavel V Afonine, Matthew L Baker, Gábor Bunkóczi, Vincent B Chen, Tristan I Croll, Bradley Hintze, L-W Hung, Swati Jain, Airlie J McCoy, et al. Macromolecular structure determination using x-rays, neutrons and electrons: recent developments in phenix. *Acta Crystallographica Section D: Structural Biology*, 75(10):861–877, 2019.
- [49] Bee Lim, Sanghyun Son, Heewon Kim, Seungjun Nah, and Kyoung Mu Lee. Enhanced deep residual networks for single image super-resolution. In *Proceedings of the IEEE conference on computer vision and pattern recognition workshops*, pages 136–144, 2017.
- [50] Steven J Ludtke, Philip R Baldwin, and Wah Chiu. Eman: semiautomated software for high-resolution single-particle reconstructions. *Journal of structural biology*, 128(1):82–97, 1999.
- [51] Andreas Lugmayr, Martin Danelljan, Andres Romero, Fisher Yu, Radu Timofte, and Luc Van Gool. Repaint: Inpainting using denoising diffusion probabilistic models. In *Proceedings of the IEEE/CVF conference on computer vision and pattern recognition*, pages 11461–11471, 2022.
- [52] Elaine C Meng, Thomas D Goddard, Eric F Pettersen, Greg S Couch, Zach J Pearson, John H Morris, and Thomas E Ferrin. Ucsf chimeraX: Tools for structure building and analysis. *Protein Science*, 32(11):e4792, 2023.
- [53] Seungjun Nah, Tae Hyun Kim, and Kyoung Mu Lee. Deep multi-scale convolutional neural network for dynamic scene deblurring. In *Proceedings of the IEEE conference on computer vision and pattern recognition*, pages 3883–3891, 2017.
- [54] Santrupti Nerli and Nikolaos G Sgourakis. Cs-rosetta. In *Methods in enzymology*, volume 614, pages 321–362. Elsevier, 2019.
- [55] Jonas Pfab, Nhut Minh Phan, and Dong Si. Deeptracer for fast de novo cryo-em protein structure modeling and special studies on cov-related complexes. *Proceedings of the National Academy of Sciences*, 118(2):e2017525118, 2021.

- [56] Amanda L Photenhauer, Rosendo C Villafuerte-Vega, Filipe M Cerqueira, Krista M Armbruster, Filip Mareček, Tiantian Chen, Zdzislaw Wawrzak, Jesse B Hopkins, Craig W Vander Kooi, Štefan Janeček, et al. The ruminococcus bromii amylosome protein sas6 binds single and double helical alpha-glucan structures in starch. *Nature structural & molecular biology*, 31(2): 255–265, 2024.
- [57] Ryan Po, Wang Yifan, Vladislav Golyanik, Kfir Aberman, Jonathan T Barron, Amit H Bermano, Eric Ryan Chan, Tali Dekel, Aleksander Holynski, Angjoo Kanazawa, et al. State of the art on diffusion models for visual computing. *arXiv preprint arXiv:2310.07204*, 2023.
- [58] Sergei Pourmal, Evan Green, Ruchika Bajaj, Ilan E Chemmama, Giselle M Knudsen, Meghna Gupta, Andrej Sali, Yifan Cheng, Charles S Craik, Deanna L Kroetz, et al. Structural basis of prostaglandin efflux by mrp4. *Nature structural & molecular biology*, 31(4):621–632, 2024.
- [59] Ali Punjani, John L Rubinstein, David J Fleet, and Marcus A Brubaker. cryosparc: algorithms for rapid unsupervised cryo-em structure determination. *Nature methods*, 14(3):290–296, 2017.
- [60] Alexander Rives, Joshua Meier, Tom Sercu, Siddharth Goyal, Zeming Lin, Jason Liu, Demi Guo, Myle Ott, C Lawrence Zitnick, Jerry Ma, et al. Biological structure and function emerge from scaling unsupervised learning to 250 million protein sequences. *Proceedings of the National Academy of Sciences*, 118(15):e2016239118, 2021.
- [61] Herbert E Robbins. An empirical bayes approach to statistics. In *Breakthroughs in Statistics: Foundations and basic theory*, pages 388–394. Springer, 1992.
- [62] Chitwan Saharia, Jonathan Ho, William Chan, Tim Salimans, David J Fleet, and Mohammad Norouzi. Image super-resolution via iterative refinement. *IEEE transactions on pattern analysis and machine intelligence*, 45(4):4713–4726, 2022.
- [63] Sjors HW Scheres. Relion: implementation of a bayesian approach to cryo-em structure determination. *Journal of structural biology*, 180(3):519–530, 2012.
- [64] Charles D Schwieters, John J Kuszewski, Nico Tjandra, and G Marius Clore. The xplor-nih nmr molecular structure determination package. *Journal of magnetic resonance*, 160(1):65–73, 2003.
- [65] Dong Si, Spencer A Moritz, Jonas Pfab, Jie Hou, Renzhi Cao, Ligu Wang, Tianqi Wu, and Jianlin Cheng. Deep learning to predict protein backbone structure from high-resolution cryo-em density maps. *Scientific reports*, 10(1):4282, 2020.
- [66] Abhishek Singharoy, Ivan Teo, Ryan McGreevy, John E Stone, Jianhua Zhao, and Klaus Schulten. Molecular dynamics-based refinement and validation for sub-5 Å cryo-electron microscopy maps. *Elife*, 5:e16105, 2016.
- [67] Jiaming Song, Arash Vahdat, Morteza Mardani, and Jan Kautz. Pseudoinverse-guided diffusion models for inverse problems. In *International Conference on Learning Representations*, 2022.
- [68] Yang Song, Liyue Shen, Lei Xing, and Stefano Ermon. Solving inverse problems in medical imaging with score-based generative models. *arXiv preprint arXiv:2111.08005*, 2021.
- [69] Yu Sun, Zihui Wu, Yifan Chen, Berthy T Feng, and Katherine L Bouman. Provable probabilistic imaging using score-based generative priors. *arXiv preprint arXiv:2310.10835*, 2023.
- [70] Guang Tang, Liwei Peng, Philip R Baldwin, Deepinder S Mann, Wen Jiang, Ian Rees, and Steven J Ludtke. Eman2: an extensible image processing suite for electron microscopy. *Journal of structural biology*, 157(1):38–46, 2007.
- [71] John J Tanner. Empirical power laws for the radii of gyration of protein oligomers. *Acta Crystallographica Section D: Structural Biology*, 72(10):1119–1129, 2016.
- [72] Genki Terashi and Daisuke Kihara. De novo main-chain modeling for em maps using mainmast. *Nature communications*, 9(1):1618, 2018.

- [73] Thomas C Terwilliger, Paul D Adams, Pavel V Afonine, and Oleg V Sobolev. A fully automatic method yielding initial models from high-resolution cryo-electron microscopy maps. *Nature methods*, 15(11):905–908, 2018.
- [74] Brian L Trippe, Jason Yim, Doug Tischer, David Baker, Tamara Broderick, Regina Barzilay, and Tommi Jaakkola. Diffusion probabilistic modeling of protein backbones in 3d for the motif-scaffolding problem. *arXiv preprint arXiv:2206.04119*, 2022.
- [75] Singanallur V Venkatakrisnan, Charles A Bouman, and Brendt Wohlberg. Plug-and-play priors for model based reconstruction. In *2013 IEEE global conference on signal and information processing*, pages 945–948. IEEE, 2013.
- [76] Ray Yu-Ruei Wang, Mikhail Kudryashev, Xueming Li, Edward H Egelman, Marek Basler, Yifan Cheng, David Baker, and Frank DiMaio. De novo protein structure determination from near-atomic-resolution cryo-em maps. *Nature methods*, 12(4):335–338, 2015.
- [77] Robin Warstat, Mehrosh Pervaiz, Pierre Regenass, Marius Amann, Karin Schmidtkunz, Oliver Einsle, Manfred Jung, Bernhard Breit, Martin Hügle, and Stefan Günther. A novel pan-selective bromodomain inhibitor for epigenetic drug design. *European Journal of Medicinal Chemistry*, 249:115139, 2023.
- [78] Robin Warstat, Mehrosh Pervaiz, Pierre Regenass, Marius Amann, Karin Schmidtkunz, Oliver Einsle, Manfred Jung, Bernhard Breit, Martin Hügle, and Stefan Günther. A novel pan-selective bromodomain inhibitor for epigenetic drug design. *European Journal of Medicinal Chemistry*, 249:115139, 2023.
- [79] Joseph L Watson, David Juergens, Nathaniel R Bennett, Brian L Trippe, Jason Yim, Helen E Eisenach, Woody Ahern, Andrew J Borst, Robert J Ragotte, Lukas F Milles, et al. De novo design of protein structure and function with rfdiffusion. *Nature*, 620(7976):1089–1100, 2023.
- [80] David S Wishart, David Arndt, Mark Berjanskii, Peter Tang, Jianjun Zhou, and Guohui Lin. Cs23d: a web server for rapid protein structure generation using nmr chemical shifts and sequence data. *Nucleic acids research*, 36(suppl_2):W496–W502, 2008.
- [81] Kevin E Wu, Kevin K Yang, Rianne van den Berg, Sarah Alamdari, James Y Zou, Alex X Lu, and Ava P Amini. Protein structure generation via folding diffusion. *Nature Communications*, 15(1):1059, 2024.
- [82] Junyuan Xie, Linli Xu, and Enhong Chen. Image denoising and inpainting with deep neural networks. *Advances in neural information processing systems*, 25, 2012.
- [83] Dan Ye, Yi-Zhen Shao, Wen-Rui Li, Zhen-Jia Cui, Ting Gong, Jin-Ling Yang, Hai-Qiang Wang, Jun-Gui Dai, Ke-Ping Feng, Ming Ma, et al. Characterization and engineering of two highly paralogous sesquiterpene synthases reveal a regioselective reprotonation switch. *Angewandte Chemie International Edition*, 63(13):e202315674, 2024.
- [84] Jason Yim, Brian L Trippe, Valentin De Bortoli, Emile Mathieu, Arnaud Doucet, Regina Barzilay, and Tommi Jaakkola. Se (3) diffusion model with application to protein backbone generation. *arXiv preprint arXiv:2302.02277*, 2023.
- [85] Yafei Yuan, Fang Kong, Hanwen Xu, Angqi Zhu, Nieng Yan, and Chuangye Yan. Cryo-em structure of human glucose transporter glut4. *Nature Communications*, 13(1):2671, 2022.
- [86] Kai Zhang, Wangmeng Zuo, Yunjin Chen, Deyu Meng, and Lei Zhang. Beyond a gaussian denoiser: Residual learning of deep cnn for image denoising. *IEEE transactions on image processing*, 26(7):3142–3155, 2017.
- [87] Xi Zhang, Biao Zhang, Peter L Freddolino, and Yang Zhang. Cr-i-tasser: assemble protein structures from cryo-em density maps using deep convolutional neural networks. *Nature methods*, 19(2):195–204, 2022.
- [88] Yuanzhi Zhu, Kai Zhang, Jingyun Liang, Jiezhong Cao, Bihan Wen, Radu Timofte, and Luc Van Gool. Denoising diffusion models for plug-and-play image restoration. In *Proceedings of the IEEE/CVF Conference on Computer Vision and Pattern Recognition*, pages 1219–1229, 2023.

Appendix

A Log-Likelihood Functions

We define here the log-likelihood functions, as mentioned in Algorithm 1.

Structure Completion. For structure completion, we use the log-likelihood function defined in (10):

$$f(\mathbf{y}, \mathbf{z}) = -\left\| \begin{pmatrix} \mathbf{I}_m & 0 \\ 0 & 0 \end{pmatrix} \mathbf{V}^T \mathbf{z} - \mathbf{S}^+ \mathbf{U}^T \mathbf{y} \right\|_2^2. \quad (15)$$

Model Refinement. In the model refinement task, we combine three sources of information with the following three log-likelihood functions:

$$\begin{aligned} f_m(\bar{\mathbf{x}}, \mathbf{z}) &= -\left\| \begin{pmatrix} \mathbf{I}_m & 0 \\ 0 & 0 \end{pmatrix} \mathbf{V}^T \mathbf{z} - \mathbf{S}^+ \mathbf{U}^T \bar{\mathbf{x}} \right\|_2^2 && \text{(incomplete model)} \\ f_s(\mathbf{s}, \mathbf{z}) &= \log p_\theta(\mathbf{s} | \mathbf{R}\mathbf{z}, t = 0) && \text{(sequence)} \\ f_d(\mathbf{y}, \mathbf{z}) &= -\|\mathbf{y} - \mathcal{B}(\Gamma(\mathbf{R}\mathbf{z}, \mathbf{s}, \chi))\|_2^2, \text{ where } \chi \sim p_\theta(\chi | \mathbf{R}\mathbf{z}, \mathbf{s}, t = 0) && \text{(cryo-EM density)} \end{aligned} \quad (16)$$

Γ is an operator turning an all-atom model into a density map with a user-defined resolution, following the `pdb2mrc` implementation of EMAN [50]. Given $\mathbf{X} = (\mathbf{x}, \mathbf{s}, \chi) = [X_1, \dots, X_A]^T \in (\mathbb{R}^3)^A$, the Cartesian coordinates of A heavy atoms,

$$\Gamma(\mathbf{X}) : x \in \mathbb{R}^3 \mapsto \sum_{i=1}^A Z_i \exp\left(-\frac{\|X_i - x\|_2^2}{2s^2}\right) \in \mathbb{R}, \quad (17)$$

where Z_i is the atomic number of atom i and $s = \text{resolution}/(\sqrt{2}\pi)$. The norm $\|\mathbf{y} - \Gamma(\mathbf{X})\|_2^2$ is computed directly in Fourier space using Parseval’s theorem, up to a time-dependent resolution r_t .

Pairwise Distances to Structure. We use the following log-likelihood function:

$$f(\mathbf{y}, \mathbf{z}) = -\|\mathbf{y} - \|\mathbf{D}\mathbf{R}\mathbf{z}\|_2\|_2^2. \quad (18)$$

B Optimization parameters

Structure Completion. All experiments are ran for 1,000 epochs, with a learning rate λ of 0.3 and a momentum ρ of 0.9. The time schedule is linear:

$$t = 1 - \text{epoch}/1000. \quad (19)$$

Model Refinement. All experiments are ran for 4,000 epochs. The learning rates are

$$\lambda_m = 0.1, \quad \lambda_s = \begin{cases} 0 & \text{if epoch} < 3,000 \\ 1 \times 10^{-5} & \text{otherwise} \end{cases}, \quad \lambda_d = 0.01, \quad (20)$$

and all the momenta are set to 0.9. r_t is set to 5 Å for the first 3,000 epochs and linearly decreases to 1.5 Å during the last 1,000 epochs. The side chain angles (χ) are sampled every 100 epochs. The time schedule is

$$t = 1 - \sqrt{\text{epoch}/4,000}. \quad (21)$$

Pairwise Distances to Structure. All experiments are ran for 1,000 epochs, with a learning rate $\lambda = 200/n$, where n is the number of known pairwise distances, and a momentum ρ of 0.99. The time schedule is

$$t = 1 - \sqrt{\text{epoch}/1,000}. \quad (22)$$

Table 1: Information on target structures. We indicate the number of modeled residues (residues included in the atomic model provided in the PDB file) and the number of deposited residues (number of residues in the sequence). We selected all single-chain proteins from the CASP15 database. TBP = to be published.

PDB	Modeled	Deposited	Resolution	Release date	∈ CASP15	Reference
7r5b	127	127	1.77 Å	2023-02-08	No	[77]
7qum	130	130	1.50 Å	2023-03-01	No	[20]
7pzt	160	160	1.84 Å	2022-11-02	Yes	TBP
8em5	92	103	1.95 Å	2023-09-27	Yes	[17]
8ok3	121	125	1.50 Å	2023-10-25	Yes	[7]
7roa	117	136	1.82 Å	2022-10-12	Yes	[16]
8ork	460	460	1.64 Å	2023-12-06	Yes	[24]
8c6z	573	630	1.85 Å	2023-05-31	Yes	[26]
8dys	409	603	1.80 Å	2022-08-17	Yes	TBP
7uww	632	635	1.61 Å	2023-06-14	Yes	[56]
8h2n	709	821	4.41 Å	2023-10-11	Yes	[8]
7zcx	1040	1424	3.10 Å	2023-06-14	Yes	[29]
8sxa	1153	1325	3.30 Å	2024-01-17	Yes	[58]
7xkw	499	561	3.10 Å	2022-04-20	No	[83]
7wsm	464	520	3.25 Å	2022-01-30	No	[85]
7ug0	418	418	2.55 Å	2022-03-23	No	[36]

Table 2: Additional structure completion results. We compare our method to Chroma [37] with a SubstructureConditioner. We report the RMSD in Å (best of 8) and the associated Evidence Lower Bound (ELBO) provided by Chroma as a proxy for realism.

PDB (# res.)	Metric	Method	Subsampling factor						
			2	4	8	16	32	64	128
7r5b (127)	RMSD (↓)	Chroma*	0.41	1.34	3.73	9.34	15.95	16.27	–
		ADP-3D	0.10	0.47	2.21	4.47	9.45	11.54	–
7r5b (127)	ELBO (↑)	Chroma*	7.79	6.72	7.27	7.56	7.40	9.10	–
		ADP-3D	7.38	7.87	7.48	6.65	7.64	7.98	–
7qum (130)	RMSD (↓)	Chroma*	0.28	0.81	2.14	3.46	7.70	11.49	14.45
		ADP-3D	0.21	0.27	1.13	2.68	5.60	7.76	13.01
7qum (130)	ELBO (↑)	Chroma*	5.87	6.08	7.16	7.13	8.43	8.89	9.27
		ADP-3D	5.64	6.47	7.87	7.56	7.99	8.76	8.98
7pzt (160)	RMSD (↓)	Chroma*	0.50	1.61	4.82	10.36	16.15	16.81	16.93
		ADP-3D	0.23	0.67	2.64	9.39	14.26	15.47	14.07
7pzt (160)	ELBO (↑)	Chroma*	5.99	5.55	5.39	7.47	8.52	8.74	9.04
		ADP-3D	5.79	6.44	6.92	7.79	8.29	7.81	8.64

G.3 Gradient Descent for Linear Constraints

In Figure 6, we compare different gradient-based techniques for minimizing over \mathbf{z} the following objective function:

$$\mathcal{L}(\mathbf{z}) = \|\mathbf{M}\mathbf{x}^* - \mathbf{M}\mathbf{R}\mathbf{z}\|_2^2. \quad (24)$$

\mathbf{x}^* is the backbone structure of the ATAD2 protein (PDB:7qum). \mathbf{M} is a masking matrix with a subsampling factor of 2. The preconditioning strategy is described in Section 4.2. Gradient descent with preconditioning and momentum leads to the fastest convergence.

G.4 Comparison to DPS

We adapted the Diffusion Posterior Sampling (DPS) algorithm [12] to tackle the structure completion problem. The central idea of DPS is to combine a reverse diffusion step with a gradient-ascent step on the log-likelihood. Instead of computing the gradient from the iterate \mathbf{x}_t (w.r.t. \mathbf{x}_t), DPS suggests

Table 3: Results for the “structure completion” and “distances to structure” tasks on additional targets with two different priors (Chroma and RFdiffusion). We report the lowest RMSD over 8 runs and the number of outputs with less than 1.5 Å RMSD between parenthesis. We compare our method to gradient descent on the negative log-likelihood (“No prior”).

PDB	Prior	Fraction of given coordinates			Fraction of given distances	
		1/2	1/8	1/32	1/8	1/16
8em5	No prior	6.46 (0)	10.23 (0)	15.79 (0)	11.46 (0)	14.60 (0)
	RFdiffusion	1.20 (8)	3.50 (0)	16.45 (0)	1.65 (0)	4.75 (0)
	Chroma	0.09 (8)	1.57 (0)	14.26 (0)	1.29 (3)	1.86 (0)
8ok3	No prior	6.17 (0)	8.98 (0)	19.67 (0)	13.11 (0)	14.66 (0)
	RFdiffusion	1.16 (8)	3.73 (0)	18.48 (0)	3.87 (0)	9.62 (0)
	Chroma	0.10 (6)	1.58 (0)	11.43 (0)	1.10 (5)	1.19 (3)
7roa	No prior	6.69 (0)	8.59 (0)	15.16 (0)	13.75 (0)	14.59 (0)
	RFdiffusion	0.62 (8)	4.01 (0)	15.04 (0)	2.40 (0)	3.16 (0)
	Chroma	0.13 (8)	2.89 (0)	11.57 (0)	1.08 (5)	1.44 (4)
8ork	No prior	6.39 (0)	9.70 (0)	15.12 (0)	23.68 (0)	22.41 (0)
	RFdiffusion	0.98 (8)	3.47 (0)	16.67 (0)	0.87 (2)	2.29 (0)
	Chroma	0.17 (6)	1.76 (0)	15.94 (0)	1.30 (4)	1.34 (3)
8c6z	No prior	6.32 (0)	10.20 (0)	17.00 (0)	23.11 (0)	24.13 (0)
	RFdiffusion	1.16 (8)	4.13 (0)	17.78 (0)	3.69 (0)	4.12 (0)
	Chroma	0.16 (8)	2.40 (0)	15.22 (0)	1.42 (4)	1.46 (2)
8dys	No prior	6.08 (0)	9.37 (0)	14.74 (0)	18.72 (0)	19.25 (0)
	RFdiffusion	1.23 (8)	4.13 (0)	17.78 (0)	1.61 (0)	2.98 (0)
	Chroma	0.22 (3)	2.42 (0)	18.74 (0)	1.65 (0)	1.63 (0)
7uww	No prior	6.41 (0)	9.55 (0)	18.14 (0)	25.31 (0)	26.78 (0)
	RFdiffusion	1.30 (8)	4.55 (0)	21.24 (0)	1.90 (0)	3.13 (0)
	Chroma	0.15 (8)	2.67 (0)	16.12 (0)	1.48 (1)	1.47 (1)
8h2n	No prior	6.35 (0)	9.37 (0)	16.57 (0)	26.25 (0)	26.24 (0)
	RFdiffusion	1.04 (8)	4.44 (0)	20.30 (0)	4.43 (0)	5.10 (0)
	Chroma	0.17 (8)	2.22 (0)	15.59 (0)	1.49 (1)	1.52 (0)
7zcx	No prior	6.35 (0)	9.43 (0)	18.14 (0)	41.77 (0)	40.22 (0)
	RFdiffusion	1.31 (8)	4.36 (0)	22.95 (0)	6.09 (0)	5.81 (0)
	Chroma	0.21 (4)	2.36 (0)	17.33 (0)	1.99 (0)	1.74 (0)
8sxa	No prior	6.12 (0)	9.19 (0)	14.32 (0)	34.06 (0)	34.43 (0)
	RFdiffusion	0.95 (8)	4.06 (0)	15.70 (0)	1.87 (0)	2.64 (0)
	Chroma	0.19 (8)	2.02 (0)	10.78 (0)	1.65 (0)	1.86 (0)

to denoise the current estimate ($\hat{\mathbf{x}}_0 = \hat{\mathbf{x}}_\theta(\mathbf{x}_t)$) and compute the gradient from the iterate $\hat{\mathbf{x}}_0$ (w.r.t. \mathbf{x}_t). The magnitude of the gradient step is controlled by a parameter named ζ' .

We compare ADP-3D to the adaptation of DPS for the structure completion task on PDB:8ok3 with a subsampling factor of 4. We compare the distribution of final RMSDs over 64 replicas and the total runtime. We perform a sweep over ζ' for DPS. Both methods are ran over 1,000 steps. As shown in Figure 7, ADP-3D leads to more accurate reconstructions. Moreover, since ADP-3D does not need to compute gradients through the denoiser, it is approximately six times faster than DPS, per iteration.

G.5 Ablation Study for Model Refinement

In Figure 8, we analyze the importance of the different input measurements for atomic model refinement. Removing the partial atomic model leads to the largest drop in accuracy. The cryo-EM density map is the second most important measurement, followed by the generative prior and the sequence.

G.6 Influence of Resolution on Model Refinement

We use ChimeraX [52, 70] to simulate the 3D density maps of the TecA bacterial toxin (PDB:7pzt), at different resolutions. We run ModelAngelo [39] on the simulated maps, using the known sequence and the default parameters. We show our results in Figure 9. For both input resolutions (2.0 Å and 4.0 Å), our method improves on ModelAngelo’s accuracy for a fixed completeness level (and reaches a higher completeness for the same accuracy). As the resolution of the map improves (gets smaller), the completeness of the output of ModelAngelo increases and the output of ADP-3D improves.

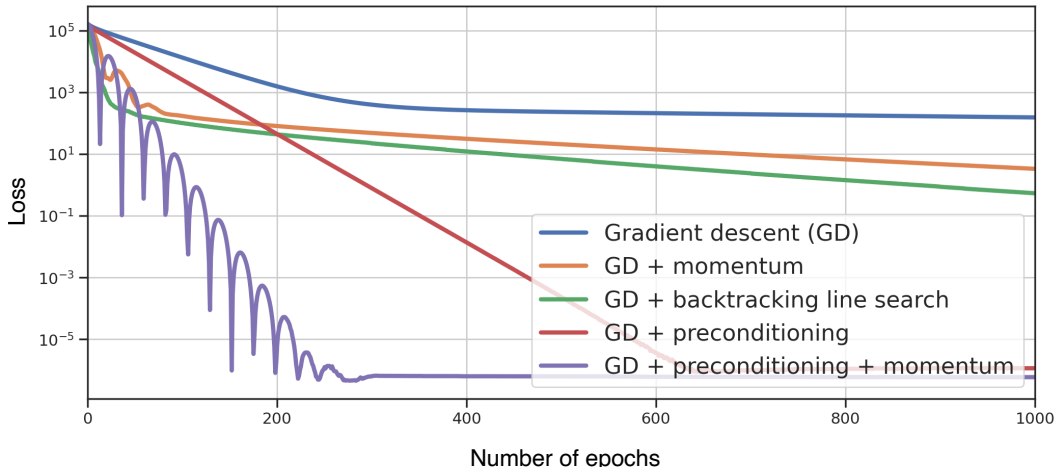


Figure 6: Gradient Descent for Linear Constraint. Convergence speed of different optimization techniques on a linear inverse problem (structure completion with a subsampling factor of 2), without the diffusion prior. Using preconditioning with momentum leads to the fastest convergence. The “loss” corresponds to the sum of squared distances between unmasked atom coordinates.

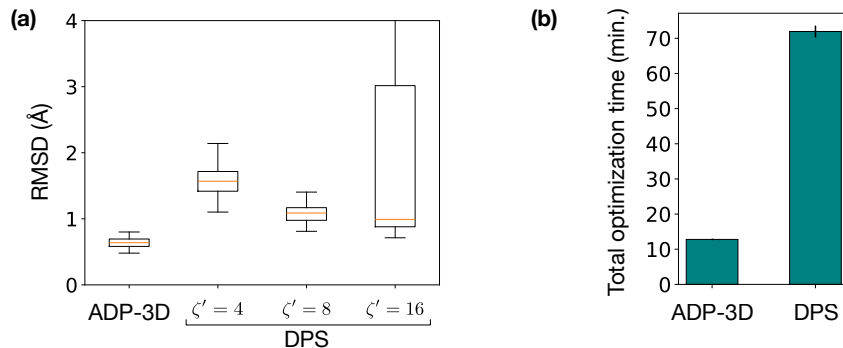


Figure 7: Comparison to DPS. We compare ADP-3D to DPS [12] for the structure completion task on PDB:8ok3, with a subsampling factor of 4. (a) Distribution of final RMSDs over 64 replicas. For DPS, we perform a sweep over the parameter ζ' , controlling the magnitude of the gradient step. (b) Comparison of runtime for the same experiment.

G.7 Variability of the Output on the Model Refinement Task

In Figure 10, we show the spread of final RMSDs obtained over 40 replicas of the same experiment (refinement of 7pzt with 2 Å density map). Some of the runs fail to reach sub-2Å RMSD, but we show that these outliers can be removed by measuring how well the structures fit into the input density map (using the log-likelihood function). This outlier removal process can therefore operate without access to ground truth information, making it straightforward to apply on new molecules.

H Additional video

We provide one additional video showing the predicted structure throughout the diffusion process, for the three tasks explored in this paper.

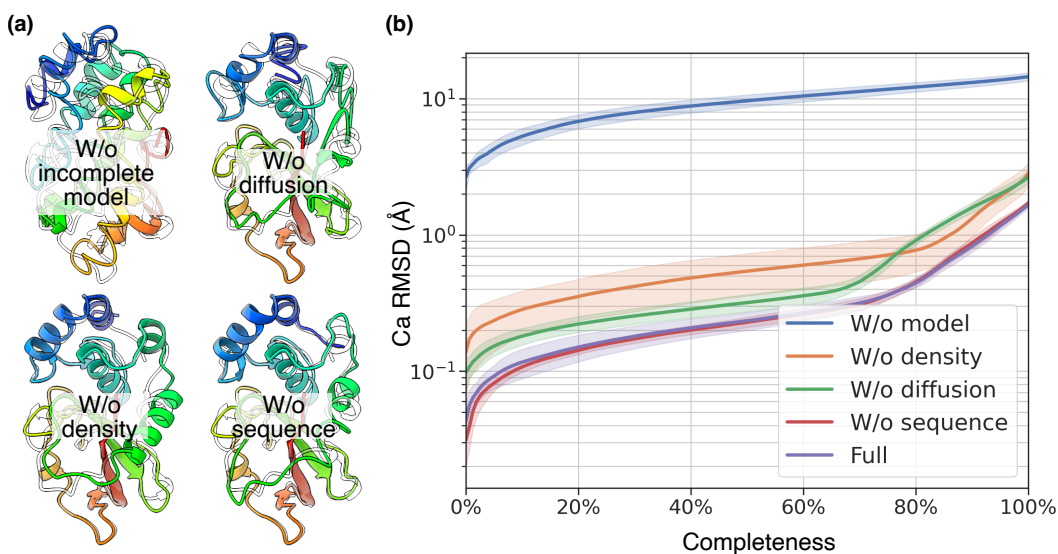


Figure 8: Ablation Study. For atomic model refinement, we combine three sources of conditioning information (incomplete model, density map and sequence) with the data-driven prior of the diffusion model. Here we highlight the importance of each conditioning information, and that of the generative prior. (a) Qualitative reconstructions with the target structure in transparency. (b) RMSD of alpha carbons vs. completeness. We use the same structure as in Fig. 4 (PDB:7pzt), and a cryo-EM map at 2.0 Å resolution.

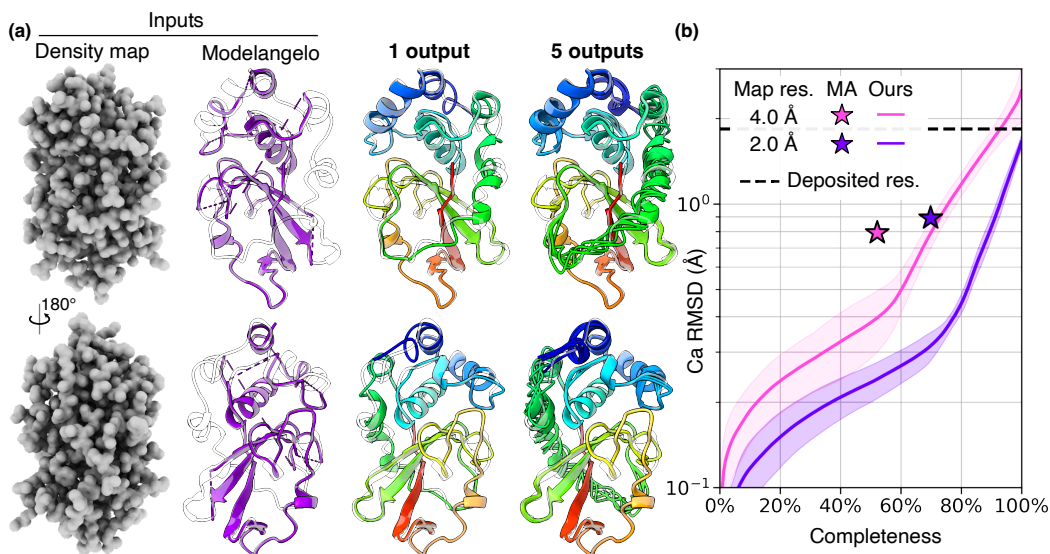


Figure 9: Atomic Model Refinement. Results on the TecA bacterial toxin (PDB:7pzt, 160 residues). (a) Qualitative results. From left to right: the input density map at 2.0 Å resolution, the incomplete model given by ModelAngelo and our refined models (1 output and 5 outputs), overlaid on the target structure in transparency. (b) RMSD of alpha carbons vs. completeness (number of predicted residues / total number of residues) with ModelAngelo (MA) and our method. We run 5 experiments and report the mean of the lowest RMSD on α -carbons over 8 replicas (± 1 std). The spread of RMSD is further described in the supplements. The experimental (deposited) resolution is indicated with a dashed line.

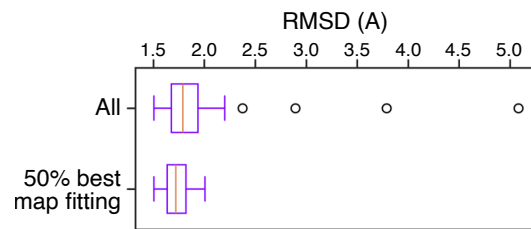


Figure 10: Spread of final C α -RMSD for the model refinement task. By filtering out the structures that least fit the input density map, we can remove outliers.